Multimodal optical imaging for detecting breast cancer

Rakesh Patel
Ashraf Khan
Dennis Wirth
Michal Kamionek
Dina Kandil
Robert Quinlan
Anna N. Yaroslavsky

Multimodal optical imaging for detecting breast cancer

Rakesh Patel,[a] **Ashraf Khan,**[b] **Dennis Wirth,**[a] **Michal Kamionek,**[b] **Dina Kandil,**[b] **Robert Quinlan,**[b] **and Anna N. Yaroslavsky**[a]

[a]University of Massachusetts Lowell, Advanced Biophotonics Laboratory, 175 Cabot Street, Suite 110-111, Lowell, Massachusetts 01854
[b]University of Massachusetts Medical School , Biotech Three, 1 Innovation Drive, Worcester, Massachusetts 01605

Abstract. The goal of the study was to evaluate wide-field and high-resolution multimodal optical imaging, including polarization, reflectance, and fluorescence for the intraoperative detection of breast cancer. Lumpectomy specimens were stained with 0.05 mg/ml aqueous solution of methylene blue (MB) and imaged. Wide-field reflectance images were acquired between 390 and 750 nm. Wide-field fluorescence images were excited at 640 nm and registered between 660 and 750 nm. High resolution confocal reflectance and fluorescence images were excited at 642 nm. Confocal fluorescence images were acquired between 670 nm and 710 nm. After imaging, the specimens were processed for hematoxylin and eosin (H&E) histopathology. Histological slides were compared with wide-field and high-resolution optical images to evaluate correlation of tumor boundaries and cellular morphology, respectively. Fluorescence polarization imaging identified the location, size, and shape of the tumor in all the cases investigated. Averaged fluorescence polarization values of tumor were higher as compared to normal tissue. Statistical analysis confirmed the significance of these differences. Fluorescence confocal imaging enabled cellular-level resolution. Evaluation and statistical analysis of MB fluorescence polarization values registered from single tumor and normal cells demonstrated higher fluorescence polarization from cancer. Wide-field high-resolution fluorescence and fluorescence polarization imaging shows promise for intraoperative delineation of breast cancers. © *2012 Society of Photo-Optical Instrumentation Engineers (SPIE).* [DOI: 10.1117/1.JBO.17.6.066008]

Keywords: breast cancer; optical imaging; reflectance; fluorescence; polarization.

Paper 12046 received Jan. 21, 2012; revised manuscript received Mar. 14, 2012; accepted for publication Apr. 13, 2012; published online Jun. 7, 2012.

1 Introduction

Breast cancer is the second leading cause of cancer-related death and the most frequently diagnosed cancer in women in the United States. Its incidence has increased considerably over the past few decades.[1,2] Breast conserving surgery (BCS) followed by radiation therapy is the preferred treatment of the early stage breast cancer. BCS provides similar survival rates to mastectomy but is less invasive and enables the woman to preserve her breast.[3] However, it is critical to obtain clear margins to minimize local recurrence and re-excision rates, which lead to increased risk to the patient, higher treatment costs, and possibly poor cosmetic outcomes.[4–6] Traditional techniques used to inspect resection margins, such as histopathology, require removal and extensive processing of the tissue. Histopathology can neither be performed on the patient in vivo, nor in real-time. Occasionally, intraoperative frozen section analysis is used for assessing tumor resection margins. This approach is time-consuming, labor intensive, doesn't evaluate the entire surgical margin, and suffers from freezing artifacts. The latter significantly decreases diagnostic utility of this method.[4,6] Most centers report a positive margin rates between 20% and 55%[7–9] for the initial surgical excision. Therefore, if a real-time accurate and cost-effective technique for intraoperative inspection of the entire resection margins were available, it would have made a rapid and major impact on the practice of surgical oncology.

Several techniques capable of noninvasive tissue interrogation are currently being investigated for the rapid and accurate demarcation of cancers through imaging or spectroscopy. They include near infrared spectroscopy, optical coherence tomography, terahertz imaging, and confocal microscopy. The results yielded by these technologies are promising. For example, terahertz imaging,[10,11] near-infrared spectroscopy,[12,13] and Raman spectroscopy[14,15] are highly sensitive to cancer, whereas optical coherence tomography,[16] and especially confocal microscopy[17] offer high-resolution morphological detail, comparable to that of histopathology. Nonetheless, the major challenge of intraoperative tumor delineation, i.e. the necessity of rapid evaluation of large surfaces, combined with high-resolution inspection of suspicious areas, has not been adequately addressed so far.

In this study, we investigated the feasibility of combining dye-enhanced macroscopic polarization imaging with multimodal confocal microscopy as a novel approach for intraoperative delineation of breast cancers. Wide-field polarization imaging allows for a rapid macroscopic overview of the entire surface area of the tissue specimen,[18,19] whereas confocal microscopy enables high-resolution imaging with a small field of view.[20] Two major types of breast cancers, including ductal and lobular carcinomas, were examined. Wide-field and high-resolution images of fresh thick breast cancer excisions stained with methylene blue (MB) were acquired. MB fluorescence polarization signals from cancerous and residual normal tissue structures were quantified and compared. The ability of the polarization macro-imaging and confocal microscopy to grossly delineate tumor margins and analyze cellular morphology, respectively, was evaluated by comparison with the gold standard of hematoxylin and eosin (H&E) histopathology.

Address all correspondence to: Anna N. Yaroslavsky, University of Massachusetts Lowell, Advanced Biophotonics Laboratory, 175 Cabot Street, Suite 110-111, Lowell, Massachusetts 01854. Tel: +978 934 1350; Fax: +978 934 1305; E-mail: yaroslav@helix.mgh.harvard.edu

2 Materials and Methods

2.1 Contrast Agents

To enhance the contrast of optical images we used a phenothiazine dye, methylene blue, which is Food and Drug Administration (FDA)-approved for human use. This dye has been successfully employed for gross-demarcation of neoplastic tumors in bladder,[21,22] pancreas,[23] and skin.[18,19] MB has also been shown to closely mimic H&E staining pattern of histopathology *in vivo*[24] and *ex vivo*.[20,25,26] For this study, commercially available methylene blue (MB 1% injection, USP, American Regent Laboratories, Inc., Shirley, NY) was diluted to a concentration of 0.05 mg/ml with Dulbecco phosphate buffered saline solution (DPBS 1×, pH 7.4, Mediatech, Mannassas, Virginia).

2.2 Sample Preparation and Handling

The experiments were performed according to the protocols approved by the Institutional Review Boards of the University of Massachusetts at Lowell and the University of Massachusetts Memorial Medical Center at Worcester. Fresh excess breast tissue was obtained following surgical resection of breast tumors at UMass Memorial Medical Center and imaged within 6 h. The size of fresh tissue samples ranged from 20 mm^2 to 150 mm^2 and the thickness from 3 to 7 mm. Specimens were soaked in 0.05 mg/ml DPBS solution of MB for approximately 10 min and then rinsed in DPBS to remove excess dye. The stained tissues were first imaged using the wide-field imaging system and then subsequently imaged with the high resolution confocal microscope. After imaging, the tissue was fixed in formalin and processed for en-face H&E paraffin embedded histopathology.

2.3 Histopathology

Horizontal histopathology sections were cut from the imaged plane of tissue samples. Five- micron thick sections were transferred to glass slides and stained with H&E in the standard way described elsewhere.[27] These H&E sections were digitized using Zeiss Axioscope microscope (Zeiss, Germany) equipped with a 5× objective lens, NA 0.13 (Zeiss, Germany) and an oil immersion 40× objective lens, NA 1.0 (Zeiss, Germany) for comparison to wide-field images and high-resolution mosaics, respectively. The optical images were correlated with histopathology obtained from approximately the same depth of the specimen.

2.4 Wide-Field Imaging

A polarization-enhanced wide-field imaging device was used to assess tumor margins on a macroscopic scale. A schematic of the system is presented in Fig. 1(a). The system has been described in detail elsewhere.[18,19] In short, a xenon arc lamp (Lambda LS, Sutter, Novanto, CA) combined with nine narrow bandpass filters, with full width at half maximum of 10 nm, that covered wavelength ranges from 390 nm to 750 nm was used as an illuminator. A 0.5× Rodenstock lens coupled to a CCD camera (CoolSnap Monochrome Photometrics, Roper Scientific, Tucson, AZ) was used for image acquisition. Linearly polarizing filters (Meadowlark Optics, Frederick, CO) were employed in pathways of the light incident on the sample and light collected by the camera. Reflectance co- and cross-polarized images were acquired at the selected wavelengths (λ = 390 nm, 440 nm, 500 nm, 577 nm,

600 nm, 620 nm, 640 nm, 680 nm, 750 nm). Fluorescence co-polarized and cross-polarized images were excited at 640 nm and registered between 660 nm and 750 nm using an additional bandpass filter (660AELP, Omega Optical, Brattleboro, VT) placed in the pathway of the light remitted from the specimen. Co- and cross-polarized images were registered with an analyzing polarizer oriented parallel (co) and perpendicular (cross) to the polarization of the incident light. In the described configuration, the system allowed for a field of view of 2.2 cm × 1.6 cm, and a lateral resolution of approximately 30 μm. The wide-field imaging of one sample required less than 3 min. For accurate detection of the two orthogonally polarized components of reflectance and fluorescence, the system was calibrated as described by Lakowicz.[28] The calibration factor, G, was determined to be 0.98.

2.5 Wide-Field Data Processing

Fluorescence polarization images were calculated using the formula:

$$I_{\text{fpol}} = \frac{If_{\text{co}} - G \times If_{\text{cross}}}{If_{\text{co}} + G \times If_{\text{cross}}}, \quad (1)$$

where I_{fpol} is a fluorescence polarization image, G is the calibration factor ($G = 0.98$), If_{co} and If_{cross} are experimental co- and cross polarized fluorescence emission images.

Reflectance polarization images were calculated using the formula:

$$I_{\text{pli}} = \frac{I_{\text{co}} - G \times I_{\text{cross}}}{I_{\text{co}} + G \times I_{\text{cross}}}, \quad (2)$$

where I_{pli} is a reflectance polarization image, G is the calibration factor ($G = 0.98$), I_{co} and I_{cross} are experimental co- and cross polarized reflectance images.

Averaged polarization values, reflectance and fluorescence, for cancerous and normal tissue regions were obtained as described elsewhere.[29] Cancerous and normal regions were grossly outlined by a pathologist in digitized histopathology slides. Due to the preparation of paraffin- embedded histopathology, sections may be stretched or shrunk in comparison to wide-field images. To correct for this artifact, digitized histopathology slides were overlaid onto wide-field images. Then affine, projective, or polynomial transformations were applied so that similar structures in the wide-field images coincided with corresponding structures in histopathology. After correction, the regions corresponding to cancer and normal breast tissue in histopathology were outlined in the wide-field reflectance and fluorescence polarization images. Mean reflectance and fluorescence polarization values for cancer and normal areas were obtained for each specimen. These values were averaged over all specimens, to obtain the mean fluorescence polarization of cancer and normal tissue.

2.6 Confocal Imaging

The schematic of the confocal microscope[24,26] that was employed for the study is presented in Fig. 1(b). Linearly polarized collimated light emitted by a 642 nm diode laser (MicroLaser Systems, Garden Grove, CA) was used for illumination. Three photomultiplier tubes (PMT R9110 Hamamatsu, Bridgewater, NJ) were used for the simultaneous multimodal signal
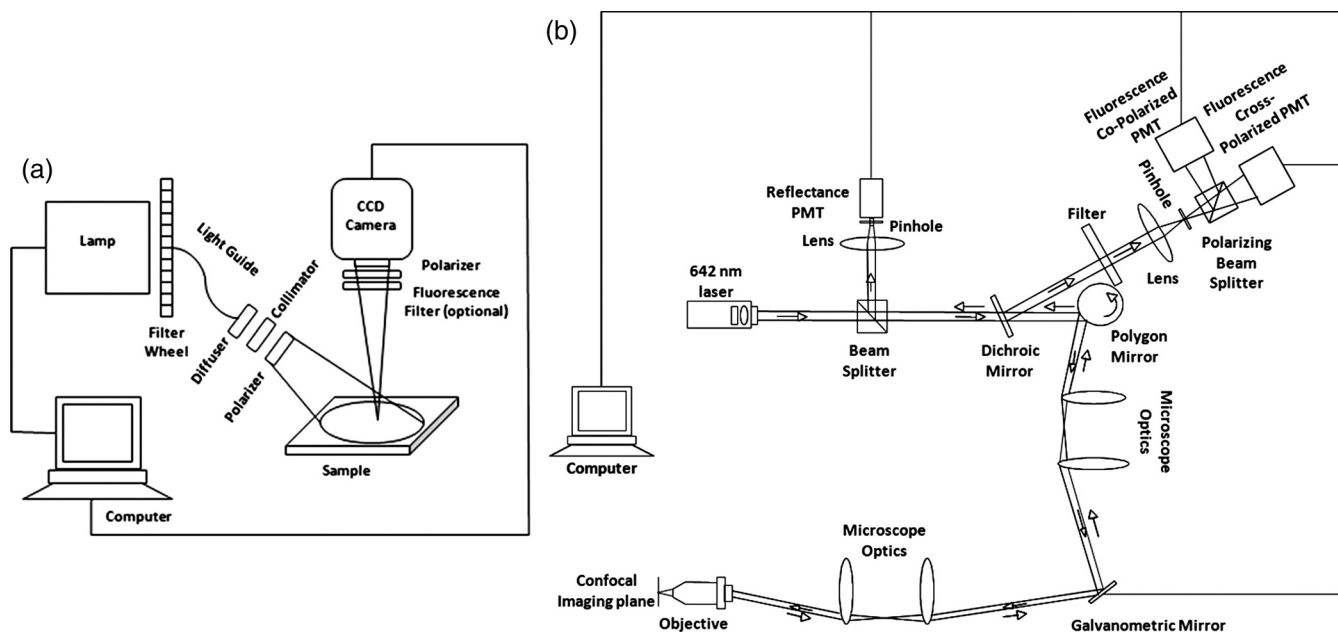
Fig. 1 Schematics of the wide-field imaging system (a) and the confocal imaging system (b).

detection, including reflectance, co- and cross-polarized fluorescence signals. This point scanning system utilized a polygon mirror (Lincoln Laser, Phoenix, AZ) for fast scanning along x-axis and a galvanometric mirror (General Scanning INC., Billerica, MA) for slow scanning along the y-axis. The signal remitted from the specimen was focused onto the 12-deg dichroic mirror (Iridian Spectral technologies, Ottawa, Ontario), which transmitted the elastically scattered and reflected fluorescence emission signal. An additional narrow bandpass filter (690 nm ± 20 nm, Chroma Technology Corp, Bellows Falls, VT) was positioned in the path of the fluorescence channel to further reject excitation light. A lens focused the fluorescence signal onto the 200 μm pinhole. Polarizing beam splitter (Karl Lambrecht Corporation, Chicago, IL) divided co- and cross-polarized fluorescence emission into their respective PMT's. The reflectance signal was deflected by a non-polarizing 95/5 beam splitter (CVI Melles Griot, Albuquerque, NM) and focused onto the 200 μm pinhole of the reflectance channel PMT by a lens. An Olympus air-immersion $40 \times /0.6$ NA and water immersion $40 \times /1.15$ NA lenses were used for imaging. The system provided a field of view of 350 $\mu m \times 350 \ \mu m$, an axial resolution of 3–6 μm, and a lateral resolution better than 0.9 μm in the range from 600 nm to 830 nm. The confocal system exhibited different efficiencies for the detection of different polarization states of the light. To enable accurate quantitation of the fluorescence polarization, the imager was calibrated in a standard manner as described elsewhere.[28] The calibration factor, G, for the confocal system was determined to be 1.2. Reflectance and fluorescence images were acquired simultaneously at a rate of 9 frames per second.

2.7 Confocal Data Processing

To locate the areas for evaluation of confocal fluorescence polarization, the pathologist selected well defined cancer and normal areas in the histopathology and corresponding confocal images. Even though exact registration of confocal and histology images is not feasible, the similarities in the H&E and MB staining

patterns allowed for the straightforward correlation. Only the cells from the innermost parts of the selected areas were used for the analysis. To calculate MB fluorescence polarization exhibited by cancer and normal cells we manually outlined well defined cancer and normal cells in the confocal fluorescence co- and cross- polarized images, averaged the pixel values across the cell area, and applied fluorescence polarization Eq. (1). Then fluorescence polarization values obtained for different types of cells were grouped by the type (cancer and normal) and averaged. Averaged fluorescence polarization values of cancerous cells were compared with those of normal cells.

2.8 Statistical Analysis

To quantify the significance of differences between the fluorescence polarization values of cancerous and normal breast tissue, we statistically evaluated the data using a one-tailed student's t-test for two independent populations. Significance tests were performed on wide-field and confocal fluorescence polarization data. For wide-field imaging mode, we tested the alternative hypothesis that the mean fluorescence polarization value averaged over cancer regions of the specimens was greater than that averaged over the normal regions of the specimens. The analysis was performed separately for ductal and lobular carcinomas, as well as for all the samples investigated. For confocal imaging mode, we analyzed the statistical significance of the fluorescence polarization differences between cancer and normal cells for one ductal carcinoma specimen.

3 Results and Discussion

3.1 Selection of Imaging Modes

In total, 17 samples were imaged, of which there were 12 ductal carcinomas (11 invasive and one intracystic papillary *(in-situ)* carcinoma) and five lobular carcinomas (all invasive). Wide-field optical images of a representative sample with ductal carcinoma are presented in Fig. 2. This is intracystic papillary

carcinoma, which remains confined within the breast ducts. Reflectance and reflectance polarization images acquired at 440 nm are shown in Fig. 2(a) and 2(d), respectively. As 440 nm lies outside the absorption band of MB, reflectance images registered at this wavelength look similar to those of unstained tissue. Comparison of reflectance [Fig. 2(a)] and reflectance polarization [Fig. 2(d)] images demonstrates that optical sectioning afforded by polarization imaging significantly improves the resolution and level of detail discernable in the image. All backscattered photons may contribute to the conventional reflectance image, whereas only single backscattered photons form the reflectance polarization image. The depth of polarization imaging is defined by the inverse of the reduced scattering coefficient of breast tissue.[20] Using optical properties of bloodless breast tissue reported in the literature,[30] we have estimated the imaging depth of polarization macro-imaging to be approximately between 320 μm–620 μm in the visible spectral range.

The 640 nm reflectance images [Fig. 2(b) and 2(e)] show increased uptake of the dye within the tumor, which results in stronger attenuation of remitted light within the MB absorption band. Similarly to the reflectance images acquired at 440 nm [Fig. 2(a) and 2(d)], the 640 nm reflectance polarization image [Fig. 2(e)] provides higher resolution, relative to the conventional reflectance image [Fig. 2(b), 640 nm]. However, comparison to histopathology presented in Fig. 2(g) demonstrates that smaller ducts with tumor, marked with dashed arrows in histopathology, were not revealed in reflectance images as they were concealed by the highly scattering connective tissue.

Wide-field fluorescence emission and fluorescence polarization images of the intracystic papillary carcinoma are presented in Fig. 2(c) and 2(f). Fluorescence emission image [Fig. 2(c)] shows that although dye uptake in the tumor is higher as compared to normal tissue, the concentration of MB in normal areas is considerable. As a result, the wide-field fluorescence emission image [Fig. 2(c)] does not allow for reliable delineation of cancer. In contrast, fluorescence polarization image [Fig. 2(f)] clearly demarcates a large tumor mass, as well as smaller tumor nests (dashed arrows). These smaller tumor nests are clearly defined only in the fluorescence polarization image [Fig. 2(f)].

Comparison of the images presented in Fig. 2(a)–2(f) demonstrate that the level of detail provided by wide-field polarization reflectance and fluorescence imaging is critical for adequate correlation to histopathology and accurate tumor demarcation.

3.2 Wide-Field Examination of Breast Cancers

Invasive ductal carcinoma is the most frequently observed type of breast cancer. This cancer is characterized by abnormal proliferation of breast ducts and infiltration of the malignant glands into the surrounding residual breast normal tissue. Wide-field images of a representative sample with grade III invasive ductal carcinoma are presented in Fig. 3. The 440 nm reflectance polarization image [Fig. 3(a)] indicates higher scattering of the tumor relative to adipose tissue. Reflectance polarization image acquired at 640 nm [Fig. 3(b)] demonstrates preferential accumulation of MB in the tumor as compared to adipose tissue. Fluorescence polarization image, presented in Fig. 3(c), reveals a large tumor mass bordered by pockets of adipose tissue, which appear dark due to the low uptake of MB. Comparison with histopathology, presented in Fig. 3(d), shows that all three images, i.e., 440 nm reflectance polarization, 640 nm reflectance polarization, and fluorescence polarization, correctly delineate
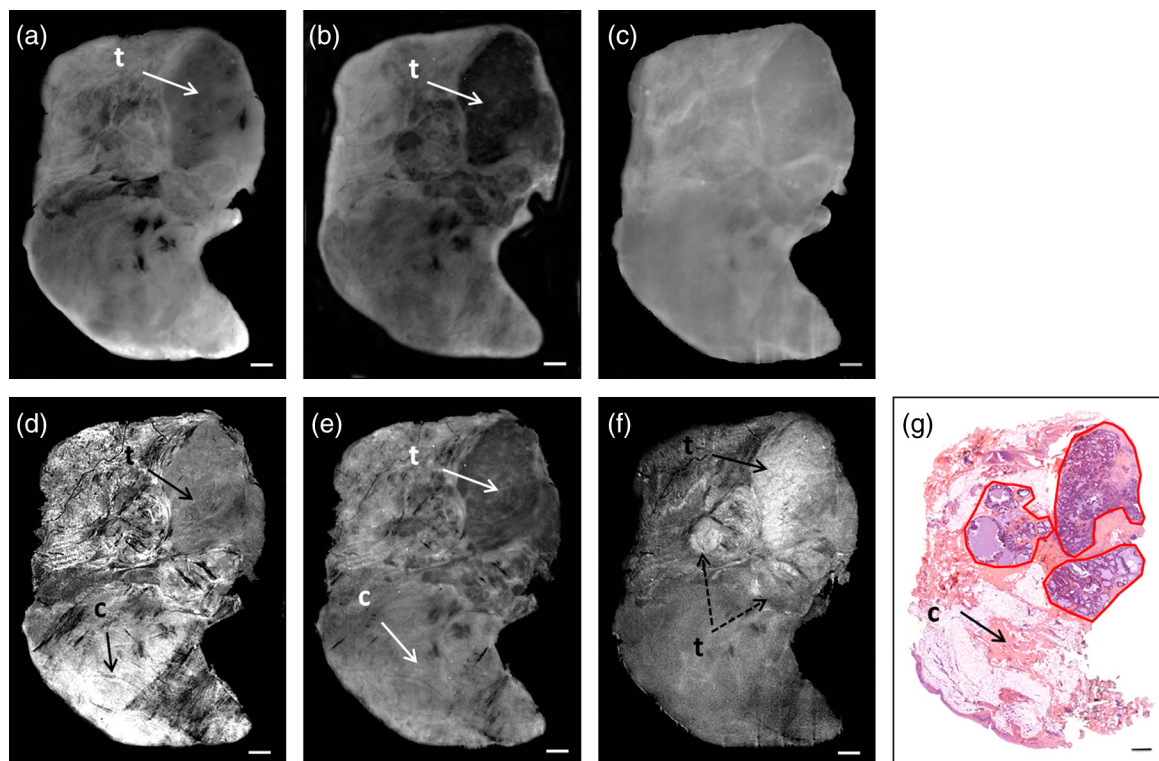

Fig. 2 Wide-field optical and histopathology images of a representative sample with intracystic papillary carcinoma; t: tumor; c: connective tissue; scale bar: 1 mm. (a) Reflectance (440 nm). (b) Reflectance (640 nm). (c) Fluorescence emission. (d) Reflectance polarization (440 nm). (e) Reflectance polarization (640 nm). (f) Fluorescence polarization. (g) Histopathology (tumor outlined in red).
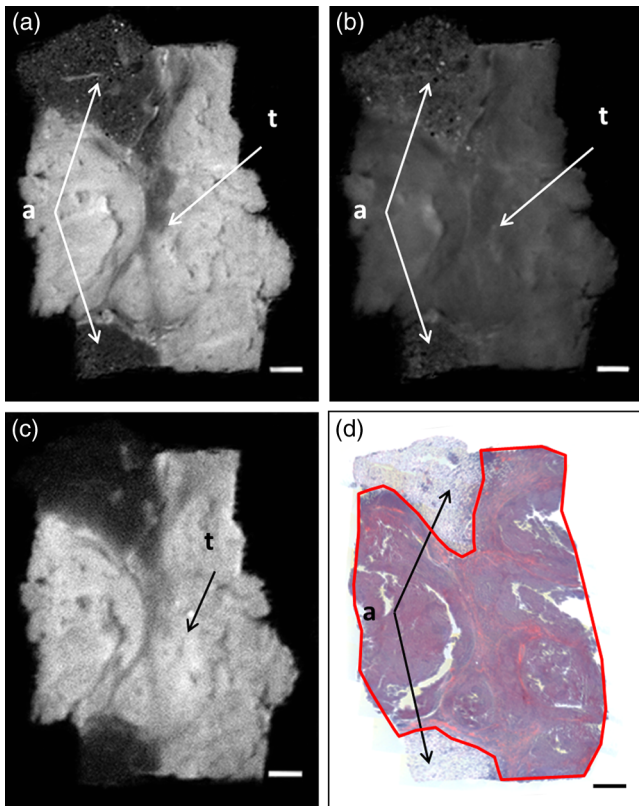
Fig. 3 Wide-field optical and histopathology images of a representative sample with grade III invasive ductal carcinoma; t: tumor; a: adipose tissue; scale bar: 1 mm. (a) Reflectance polarization (440 nm). (b) Reflectance polarization (640 nm). (c) Fluorescence polarization. (d) histopathology (tumor outlined in red).

Fig. 4 Wide-field optical and histopathology images of a representative sample with invasive lobular carcinoma; t: tumor; c: connective tissue; a: adipose tissue; scale bar: 1 mm. (a) Reflectance polarization (440 nm). (b) Reflectance polarization (640 nm). (c) Fluorescence polarization. (d) Histopathology (tumor outlined in red).

tumor margins. The size, shape and location of cancer nodules in reflectance and fluorescence polarization images correlate well with those identified in the H&E histopathology. However, due to high absorption of MB and low scattering of adipose tissue, 640 nm reflectance polarization image exhibits lower contrast as compared to 440 nm reflectance polarization and fluorescence polarization images. Due to higher scattering, which warrants better optical sectioning, 440 nm reflectance polarization facilitates higher resolution as compared to fluorescence polarization image. At the same time, due to very low MB uptake of adipose tissue, fluorescence polarization image [Fig. 3(c)] provides higher contrast as compared to the 440 nm reflectance polarization image [Fig. 3(a)].

Invasive lobular carcinoma is the second most common form of breast cancer. It typically infiltrates as tumor cells arranged in single files surrounded by a fibrous stroma and may not form a discrete mass. This type of breast cancer is therefore more difficult to delineate due to the diffuse infiltrative pattern of growth. Wide-field images of a representative specimen with invasive lobular carcinoma are presented in Fig. 4. Wide-field reflectance polarization imaging at 440 nm [Fig. 4(a)] revealed fibrous, adipose, and connective tissue structure. Comparison to the corresponding H&E section, shown in Fig. 4(d), demonstrates that 440 nm reflectance polarization image does not allow for the detection of the tumor. The 640 nm reflectance polarization image [Fig. 4(b)] highlighted areas of increased dye uptake. However, the location of these areas did not correlate well with location of cancer areas in histopathology [Fig. 4(d)]. In contrast,
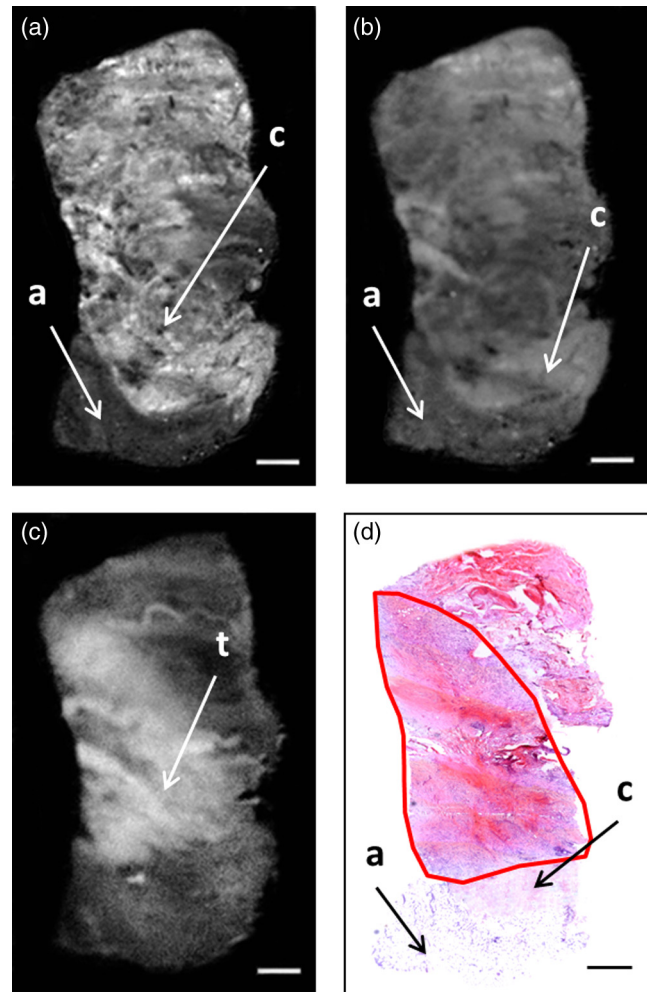
the fluorescence polarization image [Fig. 4(c)] clearly outlines the large tumor bordering connective and adipose tissue. The location, size and shape of cancer correlate well with those in histopathology. Out of the three optical images [Fig. 4(a)–4(c)], fluorescence polarization provides the best correlation with histopathology and offers the highest contrast of the tumor with respect to normal tissues.

3.3 High-Resolution Confocal Imaging

Confocal fluorescence emission mosaics of the ductal and lobular carcinomas examined using wide-field imaging (Figs. 3 and 4) are presented in Figs. 5 and 6. Mosaics of the entire specimens are shown in Figs. 5(a) and 6(a). Their appearance is similar to the wide-field fluorescence images shown in Figs. 4(c) and 3(c), respectively. Comparison of confocal mosaics with histopathology shows good correlation. Similarly to wide-field images, confocal mosaics grossly outline the tumor margins. However, as resolution provided by confocal microscopy is superior to that of wide-field technique, confocal images readily lend themselves to straight forward comparison with histopathology at the cellular level.
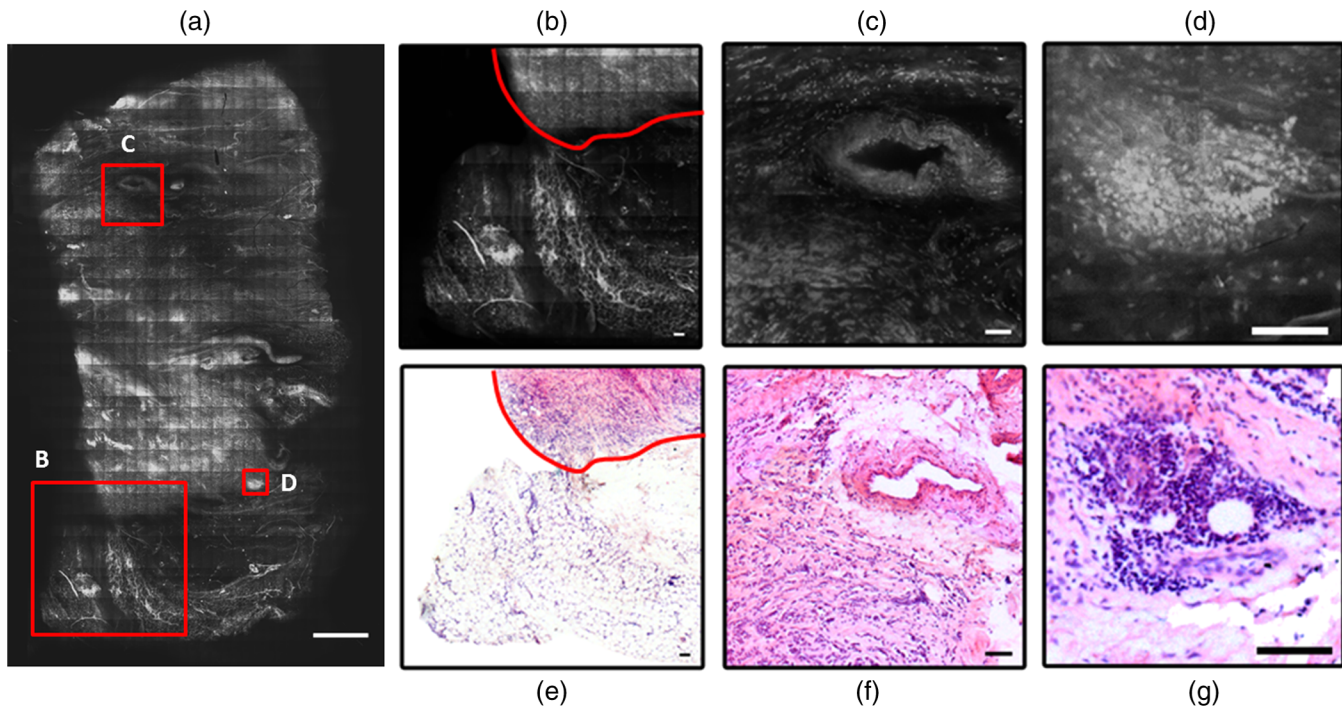
Fig. 5 Images of invasive lobular carcinoma. (a) Fluorescence emission confocal mosaic; scale bar: 1 mm. (b)–(d) Fluorescence emission confocal images from square areas outlined in (a). (e)–(g) Respective histopathology for confocal images shown in (b)–(d). Scale bars in (b)–(g): 0.1 mm.

Fluorescence emission confocal mosaics of the smaller fields within the lobular specimen outlined with squares in Fig. 5(a) are presented in Fig. 5(b)–5(d) along with corresponding histopathology shown in Fig. 5(e)–5(g). The tumor/adipose boundary can be accurately outlined in Fig. 5(b). Fat pockets separated by connective tissue, septa, as well as single cancer cells exhibit high contrast and can be clearly resolved in both fluorescence emission images [Fig. 5(b)] and histology [Fig. 5(e)]. Diffuse

tumor growth, indicative of lobular carcinoma, can be seen in Fig. 5(c), where small tumor cells are scattered around a vessel. In Fig. 5(d), confocal imaging reveals an aggregate of lymphocytes, crowded around the blood vessel. Comparison of the confocal images shown in Fig. 5(c) and 5(d) demonstrates good correlation with histopathology [Fig. 5(f) and 5(g)]. Fluorescence emission confocal mosaics of the small fields within the ductal specimen, outlined with squares in Fig. 6(a),
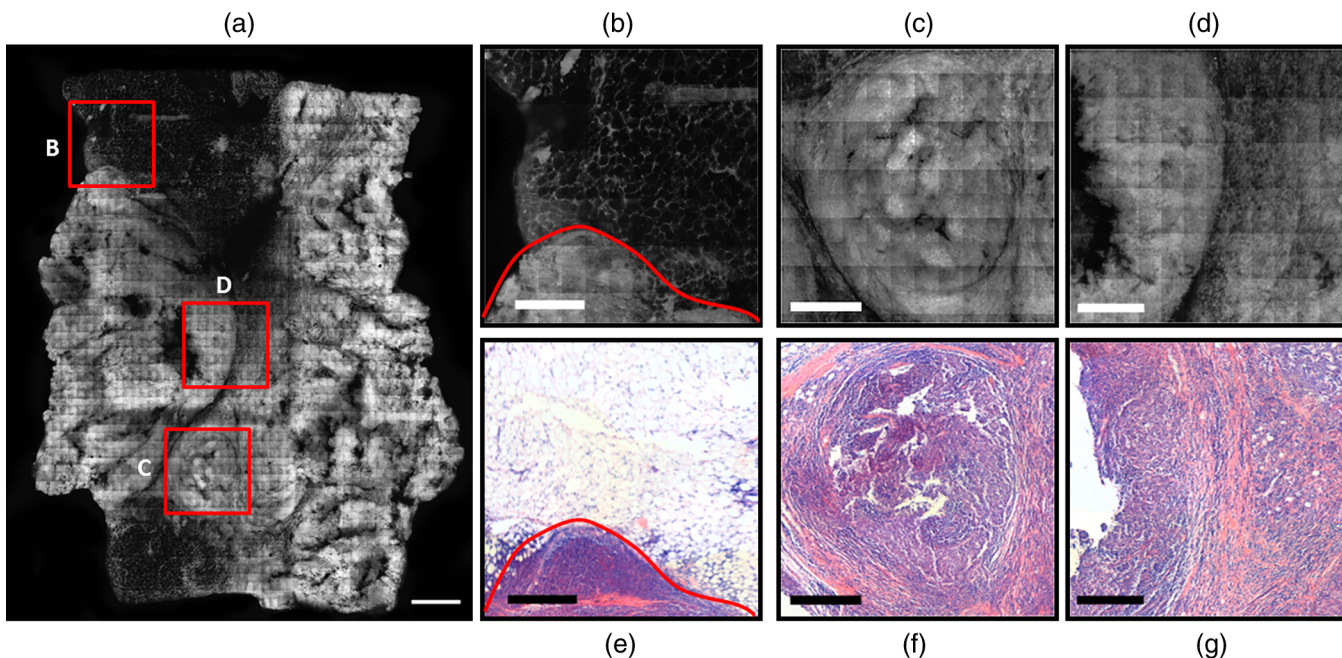

Fig. 6 Images of invasive ductal carcinoma. (a) fluorescence emission confocal mosaic. Scale bar: 1 mm. (b)–(d) Fluorescence emission confocal images from the square areas outlined in (a). (e)–(g) Respective histopathology for confocal images shown in (b)–(d). Scale bar in (b)–(g): 0.5 mm.

are presented and compared to corresponding histopathology in Fig. 6(b)–6(g). The margin between tumor cluster and adipose tissue can be accurately delineated in Fig. 6(b). Unlike cancer margins of lobular carcinoma shown in Fig. 5(a), the boundaries of ductal carcinoma do not present diffuse cancer infiltration and can be clearly outlined without analyzing cellular detail. Images presented in Fig. 6(c) and 6(d) show densely packed tumor cells, which are separated by strands of connective tissue. Close correlation between optical and histology images can be readily appreciated.

3.4 Fluorescence Polarization

Fluorescence polarization values for tumor and normal areas averaged over all samples are summarized in Fig. 7. For all the specimens investigated, wide-field fluorescence polarization exhibited by cancerous tissues higher as compared to normal tissue. More importantly, the location, shape and size of the tumor area outlined in fluorescence polarization images correlated well with those in respective histopathology. Ductal and lobular carcinomas exhibited comparable values of fluorescence polarization. Statistical analysis confirmed that the differences in fluorescence polarization averaged over tumor and normal tissue regions were significant for both ductal ($p_{ductal} < 0.00001$) and lobular ($p_{lobular} < 0.001$). A higher fluorescence polarization signal from cancer is the result of lower fluorescence depolarization of the incident signal in the tumor as compared to normal breast. Fluorescence depolarization is determined by the rotational diffusion of the fluorophore, MB, during its fluorescence life-time. Therefore, it depends on the viscosity of the environment and/or the binding state of the fluorophore. Another factor that may affect fluorescence polarization is scattering within the sample. Increased scattering yields decreased fluorescence polarization, as it randomizes polarization state of the detected signal. Both reflectance polarization images of the ductal [Fig. 3(a)] and lobular [Fig. 4(a)] carcinomas acquired at 440 nm showed that tumor affected areas were brighter than normal regions of the specimen, indicating higher scattering within the tumor. In particular, reflectance polarization values averaged over cancerous tissue are 0.14 ± 0.03 and 0.16 ± 0.06, whereas normalized reflectance polarization values averaged over normal structures are 0.08 ± 0.02 and 0.12 ± 0.04, for the ductal [Fig. 3(a)] and lobular [Fig. 4(a)] carcinomas, respectively. Analysis of the 440 nm reflectance polarization images shows that relative reflectance polarization of cancer is higher for ductal carcinoma. In particular, the averaged ratio of reflectance polarization of cancer to normal tissue for ductal carcinomas is equal to 1.8, whereas for lobular carcinoma it is equal to 1.3. Nonetheless, in both cases scattering from tumor dominates that from normal tissue. Higher scattering within the tumor should have led to lower fluorescence polarization of the signal from the tumor. In contrast our results demonstrate higher relative fluorescence polarization registered from cancer [Figs. 2(f), 4(c), and 7], even though scattering within cancer is higher than within normal tissue. This indicates that intrinsic fluorescence polarization of tumor is higher as compared to normal residual fibroadipose breast tissue. Our results reveal that binding of the fluorophore and/or viscosity within the tumor cause higher fluorescence polarization exhibited by cancer.

To evaluate fluorescence polarization on the cellular level, confocal fluorescence polarization images of a sample with invasive ductal carci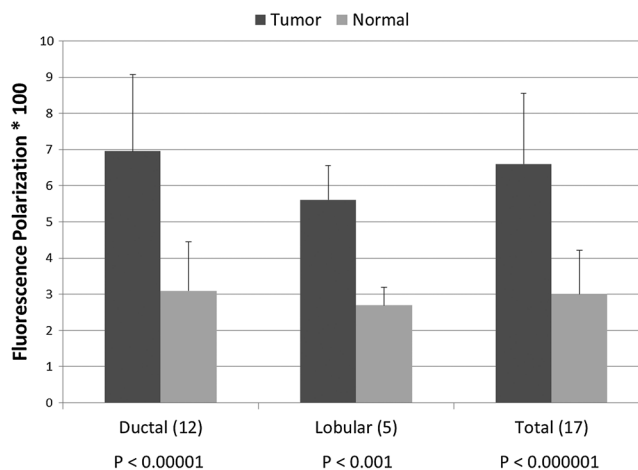noma were processed, analyzed, and compared to respective histopathology. Representative fluorescence emission and fluorescence polarization confocal mosaics of cancer and surrounding residual normal breast tissue are presented in Fig. 8(a)–8(f). Corresponding H&E histopathology is presented in Fig. 8(g)–8(i). Comparison of fluorescence emission [Fig. 8(a)–8(c)] and fluorescence polarization images demonstrates that contrast of tumor cells remains high, whereas that of normal cells decreases in fluorescence polarization. Thus, fluorescence polarization imaging may help to emphasize
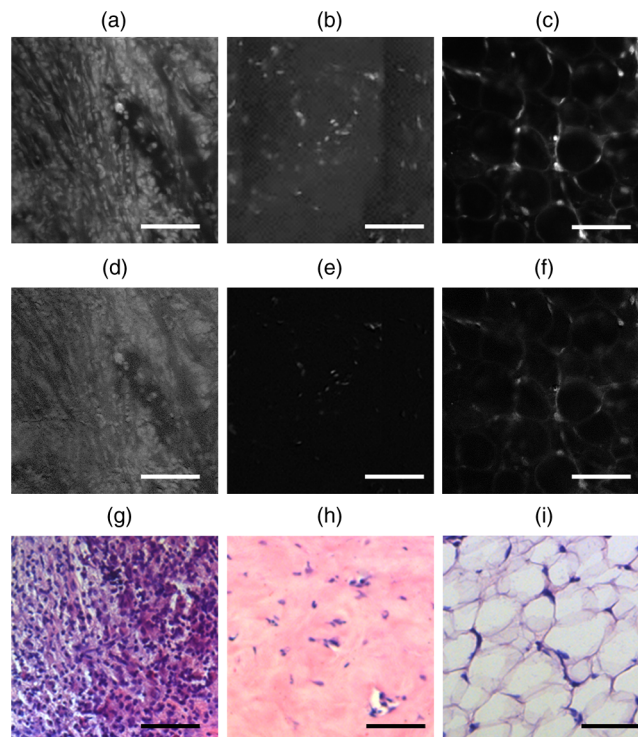

Fig. 7 Fluorescence polarization values (×100) for cancerous (dark gray) and normal (light gray) breast tissue averaged over all samples. Bars show standard deviations. *P*-values are given for student's *t*-test of two independent populations.

Fig. 8 Images of invasive ductal carcinoma; scale bar: 0.1 mm. Fluorescence emission of tumor (a), fibroblasts (b), and adipose tissue (c). Corresponding fluorescence polarization of tumor (d), fibroblasts (e), and adipose tissue (f). Histopathology of tumor (g), fibroblasts (h), and adipose tissue sections (i).
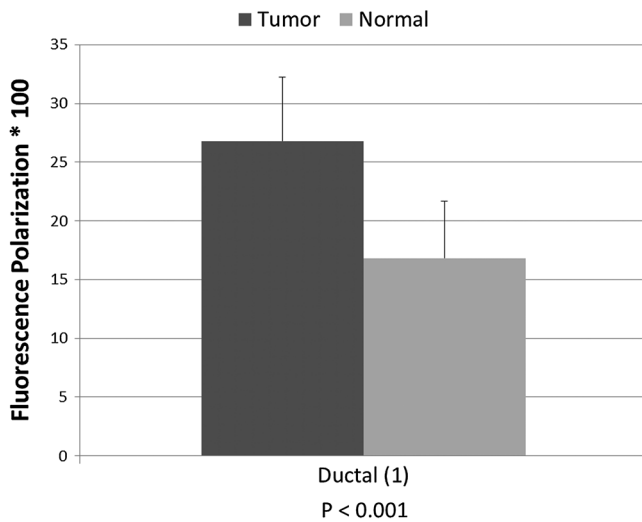
Fig. 9 Fluorescence polarization values (×100) averaged over cancer (dark gray) and normal cells (light gray) of a ductal carcinoma specimen presented in Fig. 8. Bars show standard deviations. *P* value is given for student's *t*-test of two independent populations.

cancer and distinguish tumor cells from normal. For cellular fluorescence polarization quantitation the representative areas were manually selected by comparing them with the H&E images. Only well-defined cancer and normal cells were analyzed. The analysis has shown that fluorescence polarization of tumor cells was 0.27 ± 0.05. Fluorescence polarization of normal cells was found to be 0.16 ± 0.05. Statistical test has shown that these differences are significant ($p \leq 0.001$). The results are summarized in Fig. 9. Comparison of Figs. 9 and 7, which summarizes respective results obtained from wide-field images, reveals that fluorescence polarization calculated from confocal images is higher for both cancer and normal tissue. In confocal imaging, multiple scattering does not contribute to randomization of fluorescence polarization. Therefore, the values of fluorescence polarization registered from single cancer and normal cells are higher as compared to those obtained using wide-field imaging.

4 Summary

This *in vitro* pilot study was conducted to establish the feasibility of using dye-enhanced multimodal wide-field macroscopic and high-resolution confocal imaging for intraoperative detection and demarcation of breast cancers. We acquired and analyzed reflectance, fluorescence, and polarization images of MB stained ductal and lobular carcinoma specimens. Our results indicate that topically applied aqueous solution of MB preferentially accumulates in cancer tissue and significantly enhances contrast of the optical images. Predictably, both reflectance and fluorescence wide-field polarization imaging allowed for better delineation of the superficial breast tissue structures, as compared to conventional reflectance and fluorescence emission, because polarization imaging enables optical sectioning of thick tissue. Reflectance and reflectance polarization images emphasized the structure of connective, fibrous and adipose tissues. However, in spite of considerable retention of MB in tumors, reflectance images did not delineate cancer margins reliably, most probably due to high scattering exhibited by breast tumors. In contrast, wide-field fluorescence polarization and high-resolution fluorescence emission imaging accurately

revealed the location, shape, size and morphology of tumor in all 17 specimens investigated. Fluorescence polarization of cancer, quantified from wide-field images, was reproducibly higher as compared to normal breast tissues. Similarly, as estimated from confocal images of a ductal carcinoma specimen, MB fluorescence polarization registered from cancer cells was significantly higher as compared to that of normal cells. It has been reported in the literature that MB molecules bind to mitochondria, which are plentiful in cancer cells.[31] This could explain higher fluorescence polarization signal of MB in breast tumor cells. Further studies are under way to quantify MB fluorescence polarization in cancer and normal cells and determine the possibility of using this phenomenon for detecting breast cancer.

In our study, we evaluated advantages and limitations of several complimentary reflectance, fluorescence and polarization wide-field and high-resolution imaging modalities for intraoperative breast cancer demarcation. Wide-field fluorescence polarization imaging enables rapid and accurate macroscopic delineation of breast cancer margins, but cannot provide resolution comparable to that of histopathology. Confocal fluorescence emission imaging enables microscopic analysis of the tissue morphology on the cellular level, but is limited by a less than millimeter field of view even for low 20× magnification. Acquiring multiple confocal images followed by assembling a mosaic of the entire specimen or surgical field requires considerable time. In addition, confocal mosaic represents a sizable amount of data, approximately 1.5 GB for an 8 mm × 11 mm lobular carcinoma sample imaged at 40× [Fig. 5(a)]. Besides, most of this data is not required for the delineation of cancer margins. Therefore, a combination of rapid digital imaging with confocal microscopy may enable fast, accurate and reliable intraoperative cancer demarcation, so that wide-field fluorescence polarization imaging would grossly delineate tumor margins and guide high-resolution confocal inspection of cellular detail in suspicious areas.

Optical imaging has the advantage of preserving tissue whereas in conventional histopathology valuable tissue may be lost compromising final diagnosis on permanent sections. Furthermore intra-operative frozen section evaluation of breast cancer for assessing margins may not be practical as examining the entire surface is time consuming and is not an efficient and reliable method. Additionally, optical imaging can be done in the surgical bed quickly and at a low cost thereby lowering the possibility of re-excision due to positive margins. The approach may be improved by utilizing fluorescence polarization for automated detection of breast cancer. More specimens need to be evaluated, but an accurate computer-aided diagnosis may be possible if a reproducible range of fluorescence polarization values can be established for the different breast cancer types.

Although this study analyzed tissue *ex vivo*, it will serve as a first step that will permit construction and optimization of an *in vivo* system capable of enabling complete and accurate image-guided resections of cancer. Wide-field and high-resolution fluorescence and fluorescence polarization imaging shows promise for intraoperative rapid and accurate breast cancer delineation.

References

1. Cancer facts and figures 2011 (American Cancer Society, Atlanta, 2011).
2. K. C. Chu et al., "Recent trends in U. S. breast cancer incidence, survival, and mortality rates," *J. Natl. Cancer Inst.* **88**(21), 1571–9 (1996).
3. U. Veronesi et al., "Twenty-year follow-up of a randomized study comparing breast-conserving surgery with radical mastectomy for early breast cancer," *N. Engl. J. Med.* **347**(16), 1227–1232 (2002).
4. S. E. Singletary, "Surgical margins in patients with early stage breast cancer treated with breast conservation therapy," *Am. J. Surg.* **184**(5), 383–93 (2002).
5. M. Keskek et al., "Factors predisposing to cavity margin positivity following conservation surgery for breast cancer," *Eur. J. Surg. Oncol.* **30**(10), 1058–1064 (2004).
6. E. R. Sauter et al., "Is frozen section analysis of re-excision lumpectomy margins worthwhile? Margin analysis in breast re-excisions," *Cancer* **73**(10), 2607–2612 (1994).
7. J. A. van Dongen et al., "Long-term results of a randomized trial comparing breast-conserving therapy with mastectomy: European Organization for Research and Treatment of Cancer 10801 trial," *J. Natl. Cancer Inst.* **92**(14), 1143–1150 (2000).
8. N. Bijker et al., "Risk factors for recurrence and metastasis after breast-conserving therapy for ductal carcinoma-in-situ: analysis of European Organization for Research and Treatment of Cancer Trial 10853," *J. Clin. Oncol.* **19**(8), 2263–2271 (2001).
9. L. Jacobs et al., "Positive margins: the challenge continues for breast surgeons," *Ann. Surg. Oncol.* **15**(5), 1271–1272 (2008).
10. P. C. Ashworth et al., "Terahertz pulsed spectroscopy of freshly excised human breast cancer," *Opt. Express* **17**(15), 12444–12454 (2009).
11. C. S. Joseph et al., "Continuous wave terahertz transmission imaging of nonmelanoma skin cancers," *Laser Surg. Med.* **43**(6), 457–462 (2011).
12. C. Carpenter et al., "Image-guided optical spectroscopy provides molecular-specific information in vivo: MRI-guided spectroscopy of breast cancer hemoglobin, water, and scatterer size," *Opt. Lett.* **32**(8), 933–935 (2007).
13. S. Kukreti et al., "Intrinsic near-infrared spectroscopic markers of breast tumors," *Dis. Markers* **25**(6), 281–290 (2008).
14. K. E. Shafer-Peltier et al., "Raman microspectroscopic model of human breast tissue: implications for breast cancer diagnosis in vivo," *J. Raman Spectrosc.* **33**(7), 552–563 (2002).
15. N. Stone et al., "Subsurface probing of calcifications with spatially offset Raman spectroscopy (SORS): future possibilities for the diagnosis of breast cancer," *Analyst* **132**(9), 899–905 (2007).
16. F. T. Nguyen et al., "Intraoperative evaluation of breast tumor margins with optical coherence tomography," *Cancer Res.* **69**(22), 8790–8796 (2009).
17. L. M. Schiffhauer et al., "Confocal microscopy of unfixed breast needle core biopsies: a comparison to fixed and stained sections," *BMC Cancer* **9**(1), 265–274 (2009).
18. A. N. Yaroslavsky, V. Neel, and R. R. Anderson, "Fluoresence polarization imaging for delineating nonmelanoma skin cancers," *Opt. Lett.* **29**(17), 2010–2012 (2004).
19. A. N. Yaroslavsky, V. Neel, and R. R. Anderson, "Demarcation of nonmelanoma skin cancer margins using multi-spectral polarized light imaging," *J. Invest. Dermatol.* **121**(2), 259–266 (2003).
20. M. Y. Al-Arashi, E. Salomatina, and A. N. Yaroslavsky, "Multimodal confocal microscopy for diagnosing nonmelanoma skin cancers," *Laser Surg. Med.* **39**(9), 696–705 (2007).
21. I. Fukui et al., "In vivo staining test with methylene blue for bladder cancer," *J. Urol.* **130**(2), 252–255 (1983).
22. W. B. Gill et al., "Selective surface staining of bladder tumors by intravesical methylene blue with enhanced endoscopic identification," *Cancer* **53**(12), 2724–2727 (1984).
23. I. J. Fedorak et al., "Localization of islet cell tumors of pancreas: A review of current techniques," *Surgery* **113**(3), 242–249 (1993).
24. J. Park et al., "Dye enhanced multimodal confocal microscopy for non-invasive detection of skin cancers in mouse models," *J. Biomed. Opt.* **15**(2), 26023 (2010).
25. A. N. Yaroslavsky et al., "Combining multi-spectral polarized-light imaging and confocal microscopy for localization of nonmelanoma skin cancer," *J. Biomed. Opt.* **10**(1), 014011 (2005).
26. D. Wirth et al., "Identifying brain neoplasms using dye-enhanced multimodal confocal imaging," *J. Biomed. Opt.* **17**(2), 026012 (2012).
27. "Paraffin Section Method and Technique" *IHC World*, Retrieved August 11, 2011, from http://www.ihcworld.com/_protocols/histology/parafin_section.htm.
28. J. R. Lakowicz, *Principles of Fluorescence Spectroscopy*, pp. 298–299, Kluwer Academic/Plenum Publishers, New York (1999).
29. A. N. Yaroslavsky et al., "Fluorescence polarization of tetracycline derivatives as a technique for mapping nonmelanoma skin cancers," *J. Biomed. Opt.* **12**(1), 014005 (2007).
30. N. Ghosh et al., "Measurement of optical transport properties of normal and malignant human breast tissue," *Appl. Opt.* **40**(1), 176–184 (2001).
31. A. R. Oseroff et al., "Intramitochondrial dyes allow selective in vitro photolysis of carcinoma cells," *Proc. Natl. Acad. Sci. USA* **83**(24), 9729–9733 (1986).